

Surfactant-Directed Fabrication of Supercrystals from the Assembly of Polyhedral Au–Pd Core–Shell Nanocrystals and Their Electrical and Optical Properties

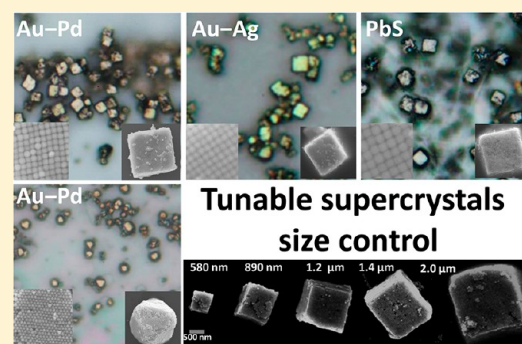
Chun-Ya Chiu,[†] Cheng-Kuang Chen,[‡] Cheng-Wei Chang,[‡] U-Ser Jeng,[§] Chih-Shan Tan,[‡] Chih-Wen Yang,[†] Lih-Juann Chen,[‡] Ta-Jen Yen,[‡] and Michael H. Huang^{*,†}

[†]Department of Chemistry and [‡]Department of Materials Science and Engineering, National Tsing Hua University, Hsinchu 30013, Taiwan

[§]National Synchrotron Radiation Research Center, 101 Hsin-Ann Road, Hsinchu Science Park, Hsinchu 30076, Taiwan

Supporting Information

ABSTRACT: Au–Pd core–shell nanocrystals with cubic, truncated cubic, cuboctahedral, truncated octahedral, and octahedral structures have been employed to form micrometer-sized polyhedral supercrystals by both the droplet evaporation method and novel surfactant diffusion methods. Observation of cross-sectional samples indicates shape preservation of interior nanocrystals within a supercrystal. Low-angle X-ray diffraction techniques and electron microscopy have been used to confirm the presence of surfactant between contacting nanocrystals. By diluting the nanocrystal concentration or increasing the solution temperature, supercrystal size can be tuned gradually to well below 1 μm using the surfactant diffusion method. Rectangular supercrystal microbars were obtained by increasing the amounts of cubic nanocrystals and surfactant used. Au–Ag core–shell cubes and PbS cubes with sizes of 30–40 nm have also been fabricated into supercrystals, showing the generality of the surfactant diffusion approach to form supercrystals with diverse composition. Electrical conductivity measurements on single Au–Pd supercrystals reveal loss of metallic conductivity due to the presence of insulating surfactant. Cubic Au–Pd supercrystals show infrared absorption at 3.2 μm due to extensive plasmon coupling. Mie-type resonances centered at 9.8 μm for the Au–Pd supercrystals disappear once the Pd shells are converted into PdH after hydrogen absorption.



INTRODUCTION

Development in the syntheses of metal and semiconductor nanocrystals with various geometric shapes has allowed the formation of supercrystals from the assembly of these nanostructures through the assistance of surfactant or capping molecules.^{1–11} Polyhedra, short nanorods, and ultrasmall spherical particles have been used as building blocks. Supercrystals can display various geometric shapes depending on the morphologies and packing arrangements of the building units. Some properties and applications of supercrystals including their use as surface-enhanced Raman spectroscopy (SERS) substrates and catalysts for organic coupling reactions have been explored.^{2,12–15} Previously, we have formed a variety of supercrystals with cubic, octahedral, rhombic dodecahedral, and branched shapes through droplet evaporation to assemble various polyhedral gold nanocrystals in the presence of cetyltrimethylammonium chloride (CTAC) surfactant.² Since particle assembly is believed to be surfactant-directed, strong evidence of surfactant residing between contacting nanocrystals should be provided. Considering the surfactant concentration as a key factor in promoting ordered nanocrystal assembly, supercrystals can also form directly in the bulk aqueous solution

through surfactant diffusion by introducing a concentrated surfactant solution over the nanocrystal solution.¹⁶ The advantage of this approach is that supercrystal formation is no longer confined to the limited area of a single droplet added to a surface. Recently, we have successfully synthesized Au–Pd core–shell, Au–Ag core–shell, and PbS nanocrystals with excellent size and shape control.^{17–20} It should be interesting to form supercrystals using these new building blocks to demonstrate that surfactant-directed nanocrystal assembly is general and broadly applicable. In addition, an interesting aspect of supercrystal formation that has never been explored is their size control, which should primarily be related to the particle and surfactant concentrations to yield optimal size. This represents a higher level of control of supercrystal formation beyond simply shape uniformity. In terms of better understanding of supercrystal properties, their electrical conductivity and optical properties are interesting to examine.

In this study, we have used various Au–Pd core–shell nanocrystals from cubes to octahedra with octahedral gold

Received: September 2, 2014

Published: January 29, 2015

cores to form polyhedral supercrystals by both droplet evaporation and surfactant diffusion methods. Cross-sectional scanning electron microscopy (SEM) and transmission electron microscopy (TEM) images were recorded by fixing a single supercrystal in position on a substrate and slicing it with focused ion beam (FIB) lithography. Low-angle X-ray diffraction (XRD), grazing incidence small-angle X-ray scattering (GISAXS), and TEM techniques were employed to confirm the presence of surfactant residing between contacting nanocrystals within a supercrystal. Tuning the temperature, nanocrystal concentration, or volumes of nanoparticle solution to surfactant solution have all been found to achieve supercrystal size control with the use of various building blocks. This represents a big step forward in the fabrication of supercrystals. Supercrystals assembled from Au–Ag core–shell cubes and PbS cubes have also been generated using the surfactant diffusion method. Electrical conductivity measurements on a single Au–Pd supercrystal were made by using two tungsten probes to contact the supercrystal. Lastly, transmittance spectra of Au–Pd supercrystals in a vacuum and hydrogen gas were recorded to examine optical properties of these supercrystals. Because hydrogen absorption into the lattice of a Pd shell forming palladium hydride can tune the refractive index of the Pd shell, a pronounced change in the spectral profile in the infrared region has been measured.^{17,21,22} These results advance our understanding of supercrystals for their possible optical and electronic applications.

■ EXPERIMENTAL SECTION

Au–Pd Nanocrystal Synthesis. The Au–Pd core–shell nanocrystals with various geometric shapes for assembly purposes were synthesized following the procedures developed in our laboratory.^{17,23} First, 97 mL of deionized water, 0.55 g of CTAB, and 2.5 mL of 0.01 M HAuCl₄ solution were added to a glass bottle. Next, 0.5 mL of 0.1 M trisodium citrate was introduced. The bottle was placed in an oven set at 110 °C. The reaction times are 4 and 6 h for making 28 and 35 nm gold octahedra (corner-to-opposite corner distance), respectively. To make Au–Pd nanocubes, both cetyltrimethylammonium chloride (CTAC) and CTAB surfactants have been used. In the synthesis of 40 nm CTAC-capped Au–Pd core–shell cubes, 8.9 mL of deionized water, 0.32 g of CTAC, and 500 μ L of 35 nm gold octahedra solution were mixed in a vial. Next, 300 μ L of 10 mM H₂PdCl₄ solution and 300 μ L of 0.1 M ascorbic acid were introduced into the vial and the solution was left undisturbed for 1 h for the growth of Pd nanocrystal shell at 30 °C. In order to synthesize 30 nm Au–Pd core–shell cubes capped with CTAB surfactant, 9.2 mL of 0.1 M CTAB solution and 500 μ L of 28 nm gold octahedra solution were mixed. Next, 200 μ L of 10 mM H₂PdCl₄ solution and 100 μ L of 0.1 M ascorbic acid were introduced into the vial and the vial was left undisturbed for 2 h at 50 °C. The reaction was stopped by centrifugation at 9000 rpm for 10 min. The procedure used to make Au–Pd particles of other shapes is similar to that used to grow cubes and is available in the Supporting Information.

Au–Ag Nanocube Synthesis. The procedure for making Au–Ag core–shell nanocubes is based on our reported method.¹⁹ First, 8.4 mL of deionized water and 1 mL of 0.1 M CTAC solution were added to a glass vial, followed by the introduction of 200 μ L of 28 nm gold octahedra and 0.3 mL of 10 mM AgNO₃ solution. Finally, 100 μ L of 0.1 M ascorbic acid was added and the solution was kept in a water bath set at 50 °C for 1 h for the growth of Ag shells. The reaction was stopped by centrifugation at 9000 rpm for 10 min. The procedure used to grow PbS nanocubes follows exactly a reported method.²⁰

Formation of Supercrystals by the Surfactant Diffusion Method. First, 10 μ L of the concentrated colloidal solution was left at the bottom of an Eppendorf tube. Then, 20 μ L of 1.0 M CTAC solution was gently introduced to keep the 1.0 M CTAC solution and colloidal solution in two layers because the CTAC solution has a lower

density than that of the colloidal solution. After 3 h, the colorful colloidal solution turned colorless and supercrystals were formed at the bottom of the tube.

To visualize the supercrystal growth process by the diffusion method, a rectangular wafer can be placed inside the tube to grow supercrystals directly on the wafer. 120 μ L of the Au–Pd colloidal solution and 240 μ L of 1.0 M CTAC solution were then introduced to the bottom of the tube. Supercrystals can be observed by optical microscope and SEM after the diffusion procedure is completed.

Formation of Supercrystals with Size Control. Formation of supercrystals by droplet evaporation and surfactant diffusion methods is described in the Supporting Information. To control the supercrystal size, concentrations of cubic, truncated octahedral, and octahedral nanocrystal solutions were diluted to 1/10 and 1/2 of that normally used by adding different volumes of 0.05 M CTAC solution. First, 1 or 5 μ L of the concentrated colloidal solution was left at the bottom of the Eppendorf tube and 9 or 5 μ L of the 0.05 M CTAC solution was transferred to the same tube for 1/10 and 1/2 dilution, respectively. The diluted solution was mixed by sonication. Subsequently, 20 μ L of 1.0 M CTAC solution was gently introduced to keep the 1.0 M CTAC solution and colloidal solution separated into two layers for gradual surfactant diffusion. For fabrication of larger supercrystals, 40 or 100 μ L of the colloidal solution was left at the bottom of the Eppendorf tube. Then, 40 or 200 μ L of 1.0 M CTAC solution was gently introduced to keep the CTAC solution and colloidal solution in two layers.

Infrared Spectroscopy of Au–Pd Supercrystals under Hydrogen Environment. Infrared spectra of supercrystals assembled by Au–Pd core–shell cubes in a vacuum and hydrogen environments were taken. Hydrogen absorption into the lattice of Pd particles forming PdH can be detected by IR spectroscopy because of the large plasmonic coupling in a supercrystal. Cubic Au–Pd supercrystals were loaded on an infrared-transparent BaF₂ substrate ($n \sim 1.46$ from 700 nm to 5 μ m), which was placed in a closed disk-shaped chamber. Air in the chamber was removed with a vacuum pump. Hydrogen was introduced from a pure hydrogen-filled balloon, which was connected to the sample chamber through a tube. After 3 min, hydrogen gas should fill the chamber. To follow the response of Au–Pd supercrystals to hydrogen absorption, a Fourier transform infrared (FTIR) spectrometer equipped with an infrared microscope was used to obtain in situ IR spectra. The measurements were performed by collecting the transmission signals before and after hydrogen absorption.

Instrumentation. SEM images of the samples were obtained using a JEOL JSM-7000F electron microscope. TEM images, high-resolution TEM (HR-TEM) images, and selected-area electron diffraction (SAED) patterns were obtained using a JEOL JEM-2100 transmission electron microscope operating at 200 kV. Optical images of the samples were taken with the use of an Olympus BX51 optical microscope with a digital camera attached. XRD patterns were acquired using a Shimadzu XRD-6000 diffractometer with Cu K α radiation. UV–vis absorption spectra were taken using a JASCO V-670 spectrophotometer. The dual-beam focused ion beam from FEI Nova-200 NanoLab Compatible was used as a “nano-knife” to prepare a series of cross-sectional surfaces of the supercrystals for SEM and TEM analysis using the lift-out approach.^{24,25} Electrical properties of supercrystals were measured by an *I–V* measurement system (Keithley Model 4200-SCS) and a four-probe nanomanipulator system (Kammrath & Wiess GmbH) installed inside a FE-SEM (JSM-7000F). FTIR spectra were recorded using an infrared microscope (Bruker Hyperion 2000, NA = 0.4). The measurements were performed by collecting the reflection and transmission signals with a HgCdTe detector over the range from 1000 cm⁻¹ (30 THz) to 4000 cm⁻¹ (120 THz). This FT-IR is also equipped with a focal plane array (FPA) to capture the image of materials. The FPA is made of arrays of bolometer receivers (detecting range: 800–12500 cm⁻¹) with 128 \times 128 pixels.

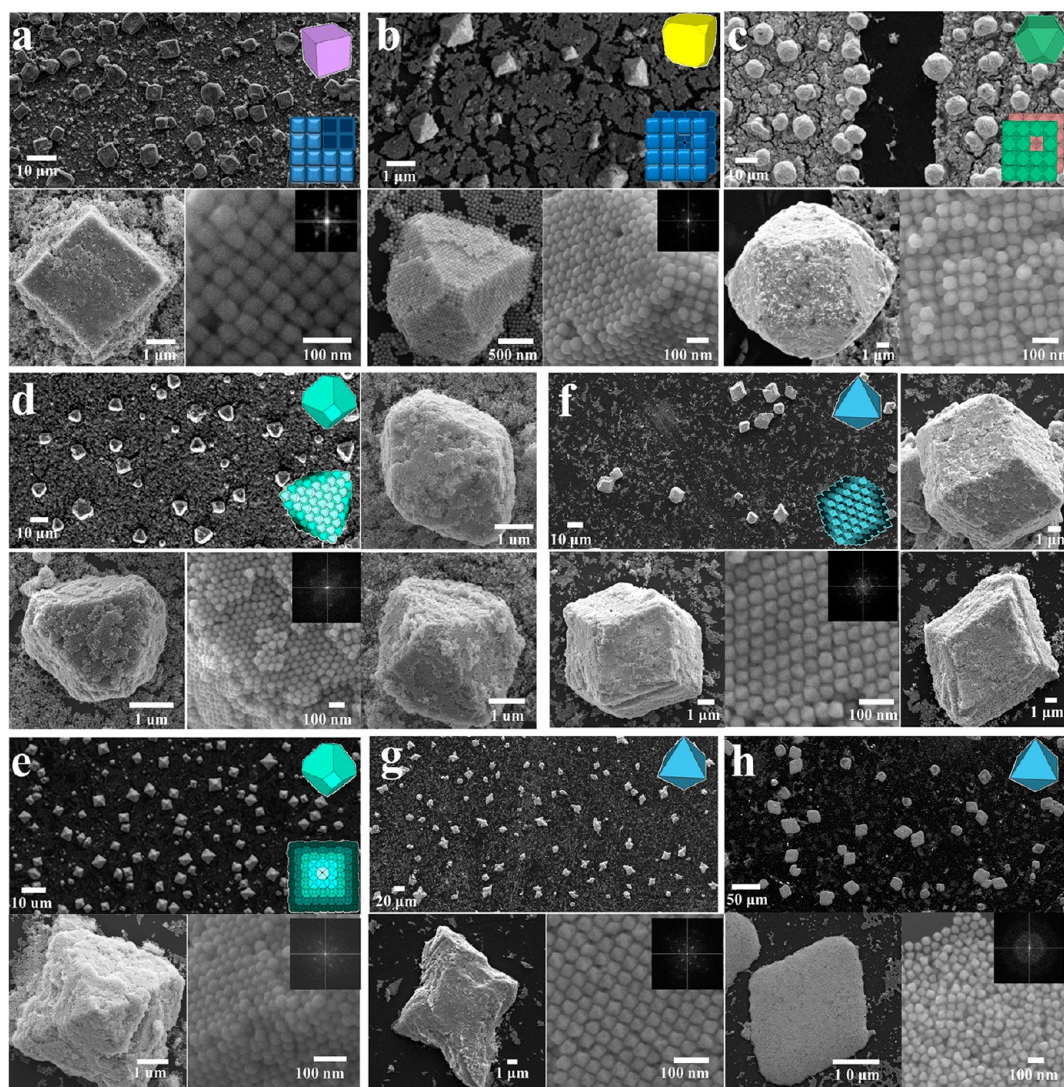


Figure 1. SEM images of supercrystals formed from various Au–Pd core–shell (a) cubes, (b) truncated cubes, (c) cuboctahedra, (d, e) truncated octahedra, and (f–h) octahedra by the droplet evaporation method. Supercrystals were generally obtained at a droplet evaporation temperature of 60 °C except for (e, f) at 90 °C and (h) at 110 °C. High-magnification SEM images show the nanocrystal packing arrangements. Models of supercrystals show the same orientation as seen in the enlarged SEM images. Insets show the corresponding Fourier transform patterns over the central regions of single supercrystals.

RESULTS AND DISCUSSION

The various Au–Pd core–shell nanocrystals were synthesized largely following our reported procedure.¹⁷ With the exception of smaller Au–Pd cubes prepared using 28 nm octahedral gold cores and CTAB surfactant, all other Au–Pd nanocrystals were made using 35 nm octahedral gold cores and CTAC surfactant. Figure S1 (Supporting Information) offers SEM images of the synthesized Au–Pd core–shell cubes, truncated cubes, cuboctahedra, truncated octahedra, and octahedra. The particles are highly uniform in size and shape with sizes in the range 35–60 nm. The smaller cubes have a size of about 30 nm. They readily self-assemble on a substrate to facilitate formation of supercrystals.

By using the droplet evaporation method with the nanocrystal droplet placed in a vial partially filled with water to slow down the evaporation rate and heated to 60, 90, and 110 °C in an oven, the various Au–Pd nanocrystals all form supercrystals with sizes of mostly 1 μm to over 10 μm. Figure 1 shows SEM images with different magnifications to see both the distribution

of supercrystals on a substrate and detailed nanocrystal packing arrangements. Au–Pd cubes formed supercrystals with a cubic shape in which the cubes position primarily right on top of another cube underneath (Figure 1a). Possibly because the cubes are less strongly locked in position, a layer of nonpacked cubes can typically be seen on the substrate. The supercrystals have sizes of $3.9 \pm 0.8 \mu\text{m}$. Corner-truncated cubes formed square pyramidal supercrystals with sizes of $1.9 \pm 0.4 \mu\text{m}$ (Figure 1b). The unique supercrystal morphology arises due to a shift in nanocube positions from one layer to the next. A truncated cube sits right at the intersection of four cubes in the lower layer. Cuboctahedra yielded cuboctahedral supercrystals on a poly(methyl methacrylate) (PMMA) substrate instead of a silicon substrate (Figure 1c). Somehow good supercrystals were not obtained when cuboctahedra were added to a clean silicon substrate. The nanocrystal packing arrangement is the same as that seen for the truncated cubes. The sizes of these cuboctahedral supercrystals are $8.8 \pm 1.0 \mu\text{m}$. At an oven temperature of 60 °C, truncated octahedra assembled into

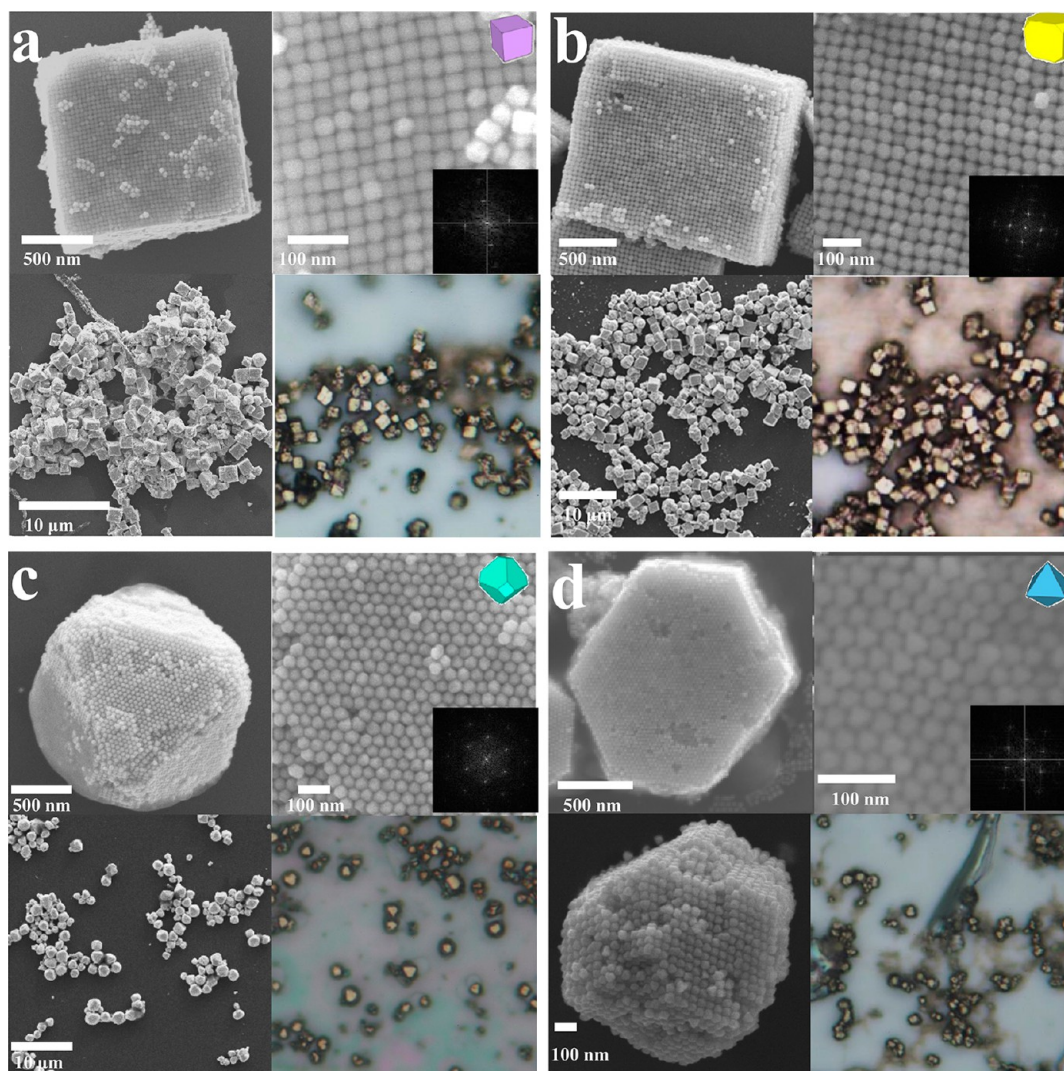


Figure 2. (a–d) SEM and optical microscopy images of Au–Pd supercrystals fabricated by the surfactant diffusion method. (a, b) Cubic and truncated cubic nanocrystals assembled into cubic supercrystals. (c) Truncated octahedra form octahedral supercrystals. (d) Octahedral nanocrystals yield supercrystals with rhombic dodecahedral and hexagonal plate shapes. Insets show the corresponding Fourier transform patterns over a single supercrystal.

supercrystals with an octahedral shape (Figure 1d). At 90 °C, they formed pyramid-shaped supercrystals (Figure 1e). Octahedra can form rhombic dodecahedral supercrystals at 90 °C (Figure 1f) and branched structures derived from a rhombic shape at 60 °C (Figure 1g). The high-magnification SEM image shown and the corresponding fast Fourier transform (FFT) pattern indicate highly ordered nanocrystal packing even at 90 °C. At 110 °C, large rhombic-shaped structures with sizes of $27 \pm 5 \mu\text{m}$ were observed, but a close examination reveals that the octahedral nanocrystals are randomly oriented.

Recognizing the formation of supercrystals should result from the growing concentrations of surfactant and nanocrystals in the solution, the surfactant diffusion method was developed by introducing a concentrated surfactant solution to a nanocrystal solution and allowing surfactant to slowly diffuse into the lower nanocrystal solution to form supercrystals (see Figure S2a, Supporting Information). The entire process occurs in aqueous solution. Here 1.0 M CTAC solution was carefully added to the Au–Pd nanocrystal solution to form two layers. After completion of the diffusion process, black precipitate forms at the bottom of the Eppendorf tube. The precipitate was

transferred to a silicon wafer for SEM imaging. Figure 2 shows SEM and optical microscopy images of Au–Pd supercrystals fabricated by the surfactant diffusion method. A large quantity of supercrystals have been produced using all nanocrystal shapes. Cubic and truncated cubic nanocrystals formed cubic supercrystals with sizes of 1.3 ± 0.2 and $1.4 \pm 0.3 \mu\text{m}$, respectively. Truncated octahedra gave octahedral supercrystals with sizes of $1.6 \pm 0.2 \mu\text{m}$. Octahedral nanocrystals yielded rhombic dodecahedral and hexagonal-shaped supercrystals. High-magnification SEM images and FFT patterns indicate high nanocrystal packing order in these supercrystals. The supercrystals have a light yellow metallic luster compared to the bright yellow appearance of Au supercrystals due to the Pd shells.² The substrate surface is clean and largely free of a layer of unpacked nanocrystals, demonstrating the advantage of using this approach to fabricate supercrystals for precise investigation of their properties. In addition, a strip of substrate can be inserted into the Eppendorf tube to deposit supercrystals on the substrate (Figure S2, Supporting Information). SEM and optical microscopy images show clearly that supercrystal size grows from the upper to lower region of the substrate, and

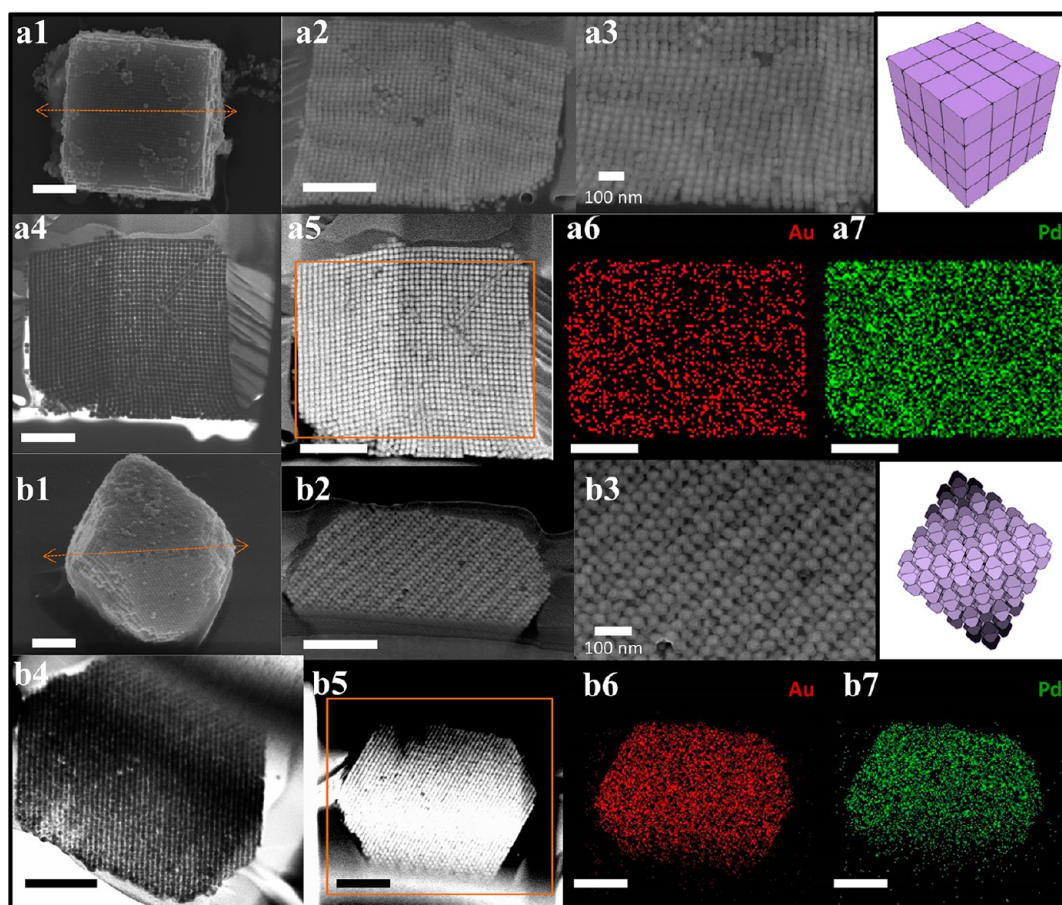


Figure 3. (a1) SEM and (a2–a4) cross-sectional SEM images of a cubic supercrystal assembled by cubic Au–Pd nanocrystals. The arrow in a1 indicates the FIB cut to obtain the sliced sample. (a5) STEM image of a cross-sectional view of a supercrystal with the rectangular region used for the EDS mapping. (a6, a7) EDS elemental mapping of Au and Pd signals. (b1) SEM and (b2, b3) cross-sectional SEM images of an octahedral supercrystal assembled by Au–Pd truncated octahedra. (b4) TEM and (b5) STEM images. (b6, b7) EDS elemental mapping. Scale bars are equal to 500 nm.

supercrystals and a layer of packed crystals coat the substrate, forming a film with varying colors.

Observation of the internal packing structure of polyhedral nanocrystals within a supercrystal is rarely available, so it is highly valuable to obtain cross-sectional images of supercrystals. A supercrystal was first fixed in position on a Si substrate by depositing a Pt protective layer. Ga ion FIB milling was employed to produce a cross-sectional cut. For TEM observation, a thin slice was made by adjusting the ion milling process from high to low current to preserve the fine internal structure and the thin slice was transferred to a TEM grid using a sample preparation approach known as the lift-out method.²⁴ Low-energy ion milling reduced the slice thickness down to 30–100 nm. Figure 3 shows cross-sectional SEM, TEM, and scanning TEM (STEM) images of cubic and octahedral Au–Pd supercrystals. The same analysis performed on a square pyramidal supercrystal assembled by Au–Pd octahedra is provided in Figure S3 (Supporting Information). Remarkably high nanocrystal packing order is present in all of these supercrystals. Their packing arrangements resemble the models shown. Clearly, the nanocrystal shapes remain intact within a supercrystal. The heights of cubic, octahedral, and pyramidal supercrystals are around 1.25, 0.7, and 3.25 μm , respectively, as judged from these cross-sectional images. Energy-dispersive X-ray spectroscopic (EDS) elemental mapping results confirm the

uniform distribution of Au and Pd signals throughout a supercrystal.

The driving force for supercrystal formation should be minimization of strong electrostatic repulsion of surfactant molecules at high concentrations by assembling nanocrystals precisely to effectively block the charges. This mechanism is similar to that used to describe the formation of mesostructured silica materials.^{26–28} Therefore, surfactant should reside in the gap space between contacting nanocrystals within a supercrystal. The evidence of their presence can be provided by taking low-angle XRD patterns of the supercrystals. Figure S4 (Supporting Information) shows low-angle XRD patterns of cubic supercrystals using CTAC and CTAB surfactants. XRD patterns of dried CTAC and CTAB were also taken for comparison. The CTAC-capped Au–Pd cubic supercrystals show several sharp peaks which are also present in the XRD pattern of dried CTAC. However, the peaks for the CTAC-capped supercrystals are shifted to lower angles in a systematic manner. The results suggest that CTAC are packed in a similarly ordered arrangement as in dried CTAC but with slightly larger d -spacing values. The same systematic shifts to lower angles are also observed in CTAB-capped Au–Pd cubic supercrystals when compared to the XRD pattern of dried CTAB. However, the magnitudes of shifts are appreciably larger for the CTAB-capped supercrystals, suggesting that the CTAB

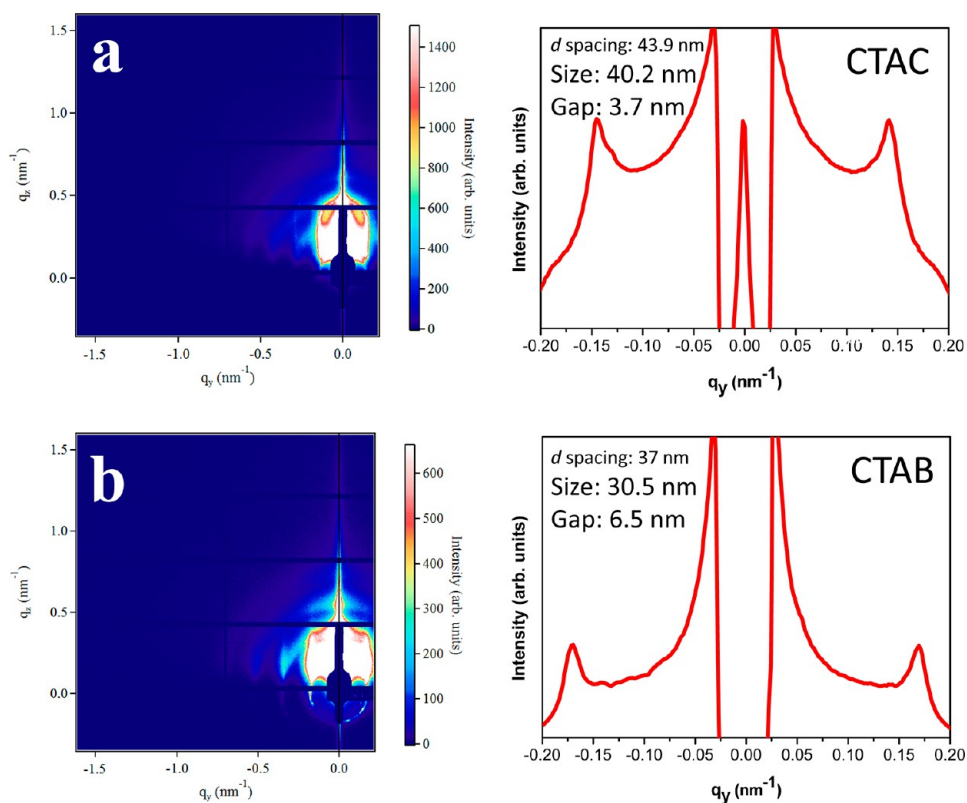


Figure 4. Experimental GISAXS images for 0.15° incidence. (a) GISAXS pattern of Au–Pd cubic supercrystals assembled from 40 nm cubes in the presence of CTAC. (b) GISAXS pattern of Au–Pd cubic supercrystals assembled from 30 nm cubes in the presence of CTAB. The d -spacing, particle size, and gap distance determined from the GISAXS patterns are provided.

molecular separation and hence particle-to-particle spacing is larger.

Due to the limitation of the small-angle XRD technique to the determination of interparticle spacing on the order of tens of nanometers, GISAXS measurements of cubic supercrystals were performed at the BL23A end station of the National Synchrotron Radiation Research Center (NSRRC) in Taiwan to determine the actual d -spacing of nanocubes and average gap size between adjacent cubes.²⁹ A detailed analysis of the diffraction image allows the determination of nanocrystal morphology, particle size, and interparticle gap width. Figure S5 (Supporting Information) gives the setup for GISAXS with the beam incident angle α and the scattering angles β and ϕ in the out-of-plane (q_z) and in-plane (q_y) directions.³⁰ Figure 4 offers the GISAXS images and patterns of cubic supercrystals assembled by 30 and 40 nm Au–Pd cubes with CTAB and CTAC surfactants, respectively. SEM images of the supercrystals and a monolayer of the cubes are given in Figure S6 (Supporting Information). From the GISAXS patterns, d -spacings of nanocrystal packing and nanocube sizes can be determined. The cube sizes match the experimentally observed particle sizes. The interparticle gap widths for CTAC- and CTAB-capped supercrystals are 3.7 and 6.5 nm, respectively. The length of fully stretched CTA⁺ is ~ 2.2 nm.³¹ Previously, a CTAB bilayer thickness of 3.2 ± 0.2 nm with partial interdigitation of the aliphatic chains was determined.³² A gap distance of 3.7 nm further proves the presence of a CTAC bilayer between contacting cubes. A CTAB bilayer distance of 6.5 nm is bigger than that normally found, which may arise from the positional adjustment of somewhat different-sized nanocubes necessary for very long-range packing. Alternatively,

the larger gap may be due to trapped surfactant micelles between the nanocrystals during nanocrystal packing. A TEM image of ordered packing of CTAB-capped nanocubes supports the existence of this gap size (Figure S6b, Supporting Information).

The above results show that surfactant mediates the formation of supercrystals. Again the driving force for the ordered assembly of nanocrystals at sufficiently high surfactant concentrations should come from the coordinated actions of bilayer structures of surfactant to pack most efficiently to minimize large polar head charges with reduced solution volume or increasing surfactant concentration as in the case of the surfactant diffusion approach. By using nearby nanocrystals to screen out the strongly positive charges from CTA⁺ and arranging them in the most stable three-dimensional structure through maximum face-to-face contact, the surfactant molecules can be densely packed and still achieve an overall stable state. The initial surfactant bilayer structure surrounding each nanocrystal should still maintain this structure when two particles are joined together, and excess surfactant is expelled into the solution.² This dynamic and responsive surfactant movement, and the corresponding nanocrystal motion to give particles the correct orientation for assembly, is also responsible for the often observed particle shape-guided effect. Thus, a significant amount of surfactant should still be present in the solution, but nanocrystals have been mostly incorporated into supercrystals when the surfactant diffusion method is used. Supercrystals with ordered packing of nanocrystals form as a result of this highly coordinated action of surfactant bilayer structure. Since nanocrystals and surfactant molecules become highly organized in a supercrystal, entropy should decrease for

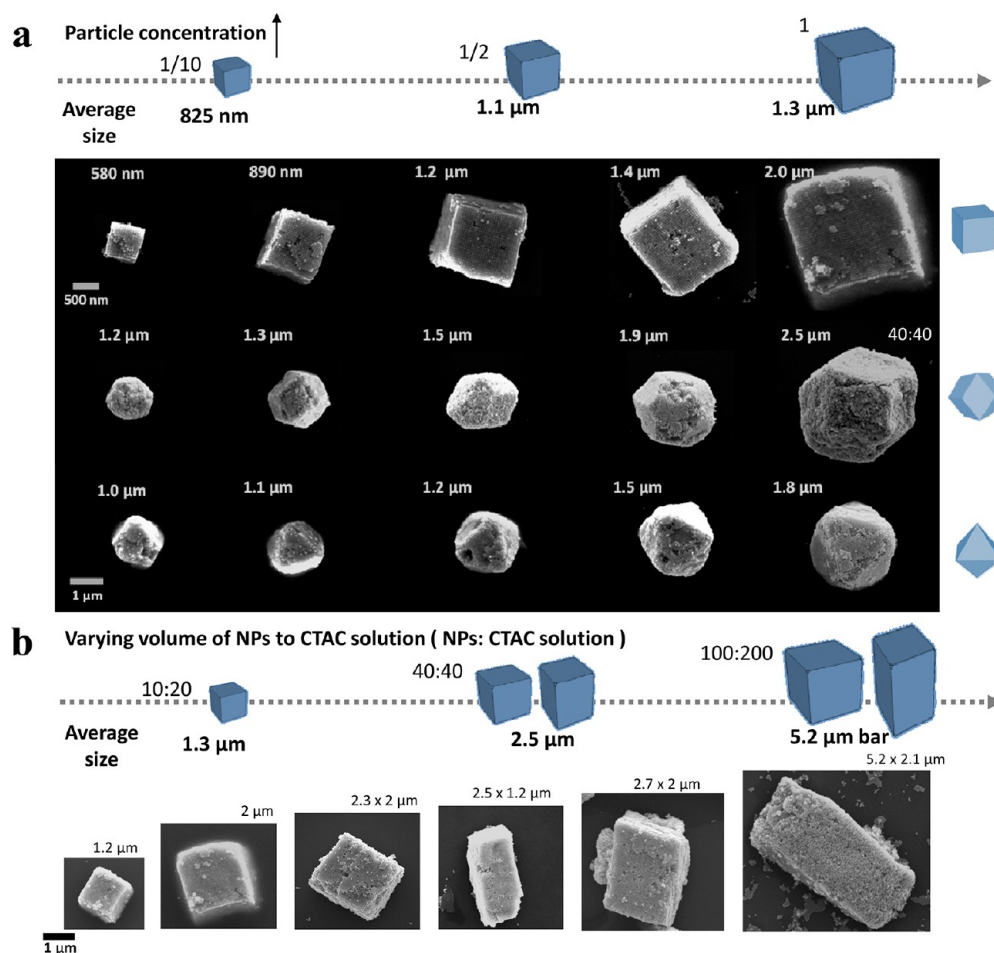


Figure 5. (a) Synthesis of cubic, octahedral, and rhombic dodecahedral supercrystals with tunable sizes by adjusting the nanocrystal concentration in the solution through dilution. Average sizes of cubic supercrystals are given. For the 2.5 μm rhombic dodecahedral supercrystal, a solution with 40 μL each of Au–Pd octahedra and CTAC was used. (b) Supercrystal size can also be tuned by varying the volumes of nanocrystal and surfactant solutions added. Supercrystal bars were generated at high nanocrystal and surfactant solution volumes. Average supercrystal sizes are given.

this process, but solvent evaporation greatly increases the overall entropy of the system. In the case of the surfactant transport approach, surfactant diffusion is entropy-increasing. Enthalpy is another important consideration, since supercrystal formation is thermodynamically favorable and happens spontaneously given proper conditions, including a sufficiently high surfactant concentration in the solution and a sufficiently long assembly time. We have learned that rapid introduction of a sufficiently large amount of surfactant into the nanocrystal solution only yields disordered particle aggregates.¹⁶ However, temperature change was hardly detectable during supercrystal formation because the process involves only surfactant reorganization, rather than bond formation or breaking. Glotzer et al. have described polyhedral nanocrystal assembly forming three-dimensional superlattice structures in solution by a directional entropic force approach.^{33–35} Depletion interactions mediated by surfactant micelles in the solution is the attractive force to pull adjacent particles together through exclusion of the micelles (depletants) from the overlapped volume between the surfactant-capped particles. A region of pure solvent without micelles creates an osmotic pressure imbalance to push the particles together. Depletion force may be applicable to supercrystal formation by bringing nearby particles together, since micelles are surely present at such high surfactant concentration. However, this mechanism may not adequately

explain the formation of supercrystals with symmetrical geometry and size control (see discussion below). Long-range and globally balanced forces should be operative to result in the formation of symmetrical supercrystals without missing corners, meaning individual particles must swiftly add to the right positions of a growing supercrystal in a coordinated fashion, and at the same time hundreds of perfect supercrystals are being formed. Slower growing supercrystals may run out of building blocks and suffer from imperfect shapes, but this is not observed. There is also the issue of how depletion force or entropic driven assembly give nanocrystals the size and shape recognition ability, such that only nanocrystals with the same shape and similar sizes are incorporated into a supercrystal; particles with different sizes and shapes form their own assembly structures when they are present in the same solution.^{2,16}

An interesting aspect of supercrystal fabrication that has never been investigated is their size control. In particular, the question is how to make progressively smaller supercrystals. Supercrystals are usually quite large with sizes of 2 μm to over 10 μm. Reducing their dimensions has the benefit of making the internal surfaces more accessible for catalytic or other applications. Size control lies on adjusting the particle and/or surfactant concentrations. Figure 5a shows that, by reducing the particle concentration to half of that normally used, supercrystal

sizes assembled from cubes, octahedra, and truncated octahedra are reduced to below $1.5\ \mu\text{m}$. Reducing the particle concentration to just $1/10$, cubic supercrystals as small as below $600\ \text{nm}$ have been generated. Remarkably, small octahedral and rhombic dodecahedral supercrystals with sizes of $1\text{--}1.2\ \mu\text{m}$ have been prepared. Large-area SEM images of the size-tunable supercrystals are shown in Figure S7 (Supporting Information). Considering that many more building blocks are needed to form supercrystals with more complex shapes as compared to cubes, these supercrystals are possibly the smallest ever reported. The ability to tune supercrystal size suggests that supercrystal formation is an extremely rapid process; simultaneous multiple supercrystal growth competing for the limited supply of nanocrystals leads to the formation of small supercrystals. We found that reduction of surfactant concentration to $1/10$ of the amount normally used does not generate supercrystals but a monolayer of nanocubes on the substrate. In addition, we found that, by raising the solution temperature to 50 or $110\ ^\circ\text{C}$ during supercrystal growth by the surfactant diffusion method, much smaller cubic supercrystals can be obtained than those formed at 17 and $30\ ^\circ\text{C}$ (Figure S8, Supporting Information). Higher temperatures may lead to more rapid nanocrystal assembly and surfactant diffusion processes, and smaller supercrystals are produced. On the other hand, when the volumes of both nanocube and CTAC solutions are increased to $40\ \mu\text{L}$ each from 10 and $20\ \mu\text{L}$ normally used, novel rectangular supercrystal microbars are formed (Figure S5b and Figure S7, Supporting Information). Further increasing nanocube and CTAC solutions to 100 and $200\ \mu\text{L}$, respectively, the microbars also increase in size. A slower assembly rate with higher nanoparticle and surfactant amounts may induce anisotropic growth of large supercrystals.

To show the generality of the surfactant diffusion method to generate diverse supercrystals, Au–Ag core–shell nanocubes and PbS nanocubes have been synthesized and assembled to form cubic supercrystals. The particles were prepared by following our reported procedures.^{19,20} Figure S9 (Supporting Information) shows TEM characterization of the synthesized $31\ \text{nm}$ Au–Ag core–shell nanocubes with octahedral Au cores. Figure 6 presents SEM and optical microscopy images of cubic supercrystals assembled by the Au–Ag core–shell nanocubes and $38\ \text{nm}$ PbS nanocubes. Good supercrystals were produced in both cases with dimensions of a few microns. Clearly, building blocks of various compositions can form supercrystals to expand their applications.

The electrical properties of supercrystals assembled by CTAC-capped $40\ \text{nm}$ Au–Pd core–shell cubes were investigated. A nanomanipulator system with surface oxide-free tungsten probes attached was used to make contact with a single supercrystal for I – V measurements. Previously, the same method was employed to make electrical conductivity measurements of single Cu_2O crystals and a Cu_2S – Ag_2S superlattice nanowire.^{36,37} Figure 7 shows SEM images of two tungsten probes contacting a single Au–Pd supercrystal with sizes of 1 and $2.2\ \mu\text{m}$ and the measured I – V curves. The supporting Si substrate was heated at $900\ ^\circ\text{C}$ in an air atmosphere in a tube furnace for $48\ \text{h}$ to form a $500\ \text{nm}$ insulating SiO_2 layer to prevent leakage current flowing from the supercrystal to the Si substrate. Essentially no current flow was measured below $3\ \text{V}$. Current rises beyond $3\ \text{V}$, but only small currents of tens of nA were recorded even at $5\ \text{V}$. The results reveal that metallic conductivity is lost with the presence of CTAC surfactant

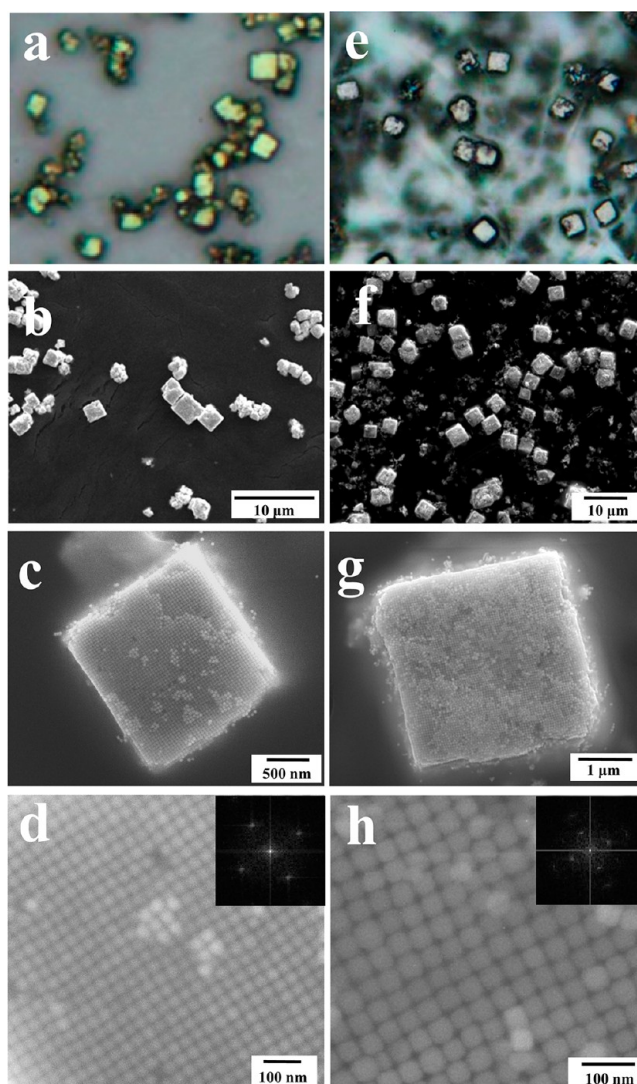


Figure 6. Supercrystals formed from the assembly of (a–d) Au–Ag core–shell nanocubes and (e–h) PbS nanocubes using the surfactant diffusion method. (a, e) optical microscope images. (b–d and f–h) SEM images of the cubic supercrystals viewed at different magnifications. Insets show the corresponding FFT patterns.

between particles. The current flow for the $1\ \mu\text{m}$ supercrystal is somewhat better than the $2.2\ \mu\text{m}$ supercrystal because a smaller supercrystal is less insulating. Current should pass across the supercrystal via tunneling among nanocrystals.

To further investigate the properties of Au–Pd supercrystals, we measured their optical properties in the infrared regime. Infrared spectra of the cubic Au–Pd supercrystals were obtained using a focal plane array coupled to a Fourier transform infrared spectrometer, as shown in Figure S10 (Supporting Information).³⁸ Ten supercrystals with similar sizes were examined. The averaged spectrum shows two obvious dips at 3.2 and $9.8\ \mu\text{m}$ for the supercrystal in air (Figure 8a). Previously, we have shown that Au–Pd core–shell nanocrystals can act as plasmonic hydrogen sensors by shifting the plasmonic band of the Au cores significantly upon absorption of hydrogen into the lattice of the Pd shell forming PdH.^{17,21} Infrared transmission spectra of the Au–Pd supercrystals in a hydrogen environment were recorded (Figure 8b). After filling the sample chamber with hydrogen, the supercrystals exhibit only one resonance at $3.3\ \mu\text{m}$. The simulated

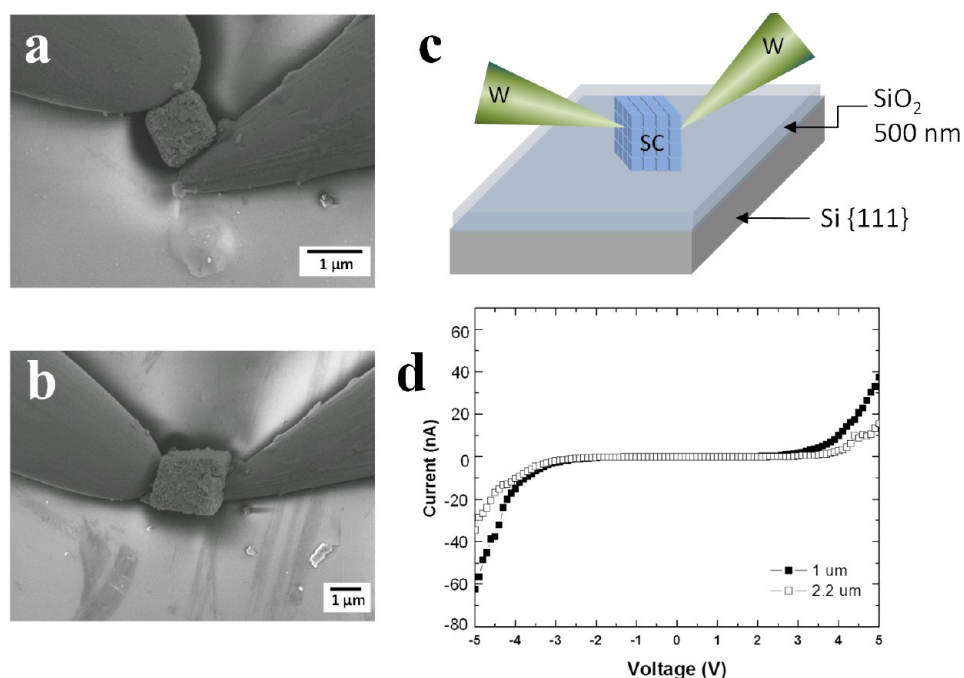


Figure 7. (a, b) SEM images showing two tungsten probes making contact to a single Au–Pd supercrystal for I – V measurements. The supercrystals have sizes of (a) 1 μm and (b) 2.2 μm . (c) Schematic drawing of the setup for I – V measurements. (d) I – V curves of these two cubic supercrystals.

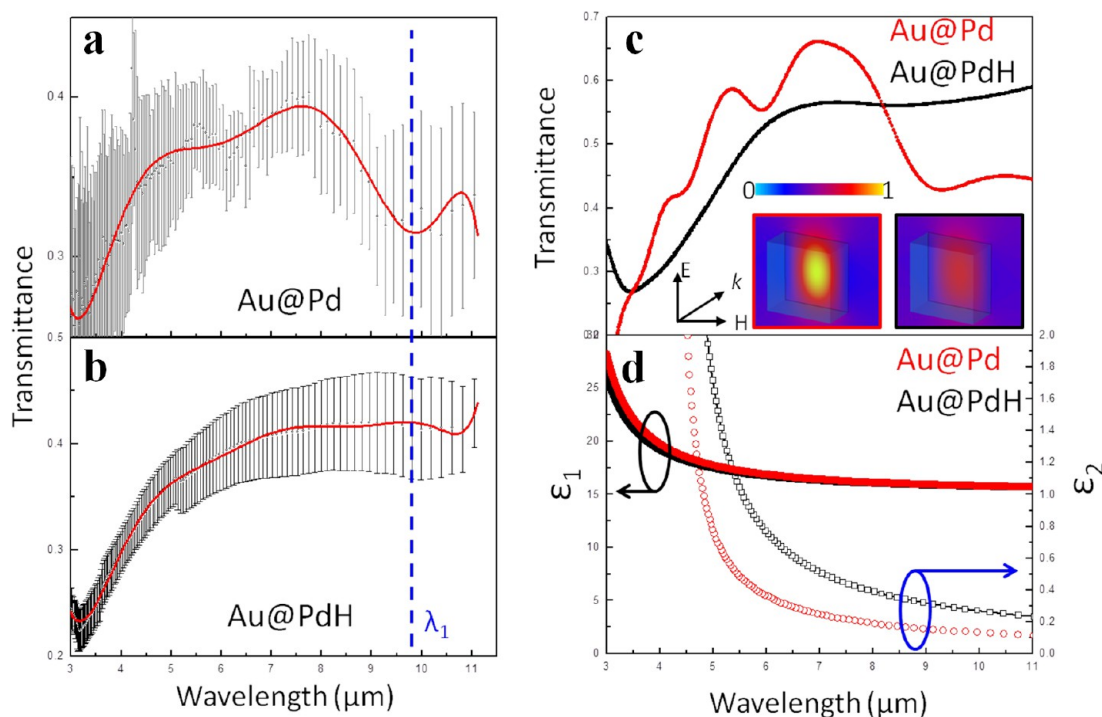


Figure 8. Measured average transmission spectra of cubic Au–Pd supercrystals with sizes of $2.5 \pm 0.3 \mu\text{m}$ (a) before and (b) after hydrogen absorption forming PdH. The errors bars are the ranges of the measured transmittance values. The red lines represent the best fit lines. (c) Simulated transmission spectra of Au–Pd supercrystals (red) and Au–PdH supercrystals (black). The insets are x -component magnetic field (H_x) distribution in Au–Pd supercrystals (red) and Au–PdH supercrystals (black) at wavelength $= \lambda_1$ indicated in panels a and b. (d) The effective dielectric functions ($\epsilon_1 + i\epsilon_2$) of Au–Pd supercrystals (red) and Au–PdH supercrystals (black).

spectra show excellent agreement with the measurements (Figure 8c). According to the effective medium theory, such a nanocrystal-built supercrystal can be simplified as a homogeneous bulk in the long wavelength region (dimensions of core-shell nanocrystals \ll wavelength of incidence). Because of the extensive plasmonic coupling present in metal supercrystals,

their optical signals should be red-shifted beyond the near-infrared range into the infrared region.^{23,39} Thus, the resonance at 3.2 μm is a collective plasmon resonance, while the resonance at 9.8 μm is a Mie resonance caused by the stacked nanocubes in a supercrystal, as shown in the inset of Figure 8c.

Figure 8d shows real (ϵ_1) and imaginary (ϵ_2) parts of effective dielectric parameters (ϵ , $\epsilon = \epsilon_1 + i\epsilon_2$) for both the Au–Pd and Au–PdH supercrystals. The supercrystals induce strong dispersive dielectric constants, resulting in great infrared light absorption and the transmission dip near the resonant wavelength at 3.2 μm . In such a strong dispersive region, the real and imaginary parts of dielectric constants are significantly shifted to ultrahigh values due to a collective plasmon response. The collective resonance is associated with the diffractive coupling of localized surface plasmon resonances (LSPR), which is significantly affected by the particle number, interparticle spacing, and filling factors. In contrast to the significant dispersive region in the collective resonance region, there are high values of effective permittivity predicted from the densely packed nanocrystals in the longer wavelength region. Such high values of permittivity suggest that the nanocrystals forming supercrystals can support Mie-type resonances and act as a magnetic-dipole mode at the resonant wavelength λ_1 ($\lambda_1 = 9.8 \mu\text{m}$), which is essentially determined by the diameter d of the supercrystal and the permittivity ϵ of its constituent material. However, comparing the strength of the magnetic-dipole mode of Au–Pd and Au–PdH supercrystals, the latter shows a very weak response due to the high loss part (ϵ_2) of the dielectric constant in Au–PdH. Thus, a tunable optical resonance in the infrared regime via Au–Pd supercrystals has been achieved, demonstrating their potential as gas-active supercrystals, tunable refractive index media,⁴⁰ and isotropic magnetic metamaterials.⁴¹

CONCLUSION

Various Au–Pd core–shell nanocrystals from cubic to octahedral structures with octahedral gold cores have been used to form excellent supercrystals with diverse morphologies by both droplet evaporation and surfactant diffusion methods. Cross section images of the supercrystals reveal the interior nanocrystals are orderly packed with preservation of their shapes. Low-angle XRD patterns, GISAXS images, and TEM images confirm the presence of CTAC and CTAB surfactants between contacting particles within a supercrystal. As an attempt to control supercrystal size, we found that, by diluting the nanocrystal concentration or increasing the nanocrystal solution temperature, supercrystal size can be tuned to well below 1 μm . Unusual rectangular microbars assembled from Au–Pd cubes have been prepared using a solution with high surfactant and nanocrystal concentrations. The broad utility of the surfactant diffusion method has been further demonstrated by making Au–Ag and PbS supercrystals. Because of the presence of surfactant, electron transport across a supercrystal is much more difficult, so metallic conductivity is lost in Au–Pd supercrystals. The cubic Au–Pd supercrystals show infrared absorption and a tunable infrared transmission profile by converting the Pd shells into PdH after hydrogen absorption, showing the potential of Au–Pd supercrystals as hydrogen-responsive structures.

ASSOCIATED CONTENT

Supporting Information

Additional experimental procedures, SEM images of Au–Pd nanocrystals, optical and SEM images of supercrystals deposited on a substrate, cross-sectional images of a square pyramidal supercrystal, XRD patterns, GISAXS configuration, TEM image of CTAB-capped array of cubes, SEM images of cubic supercrystals obtained at different temperatures, TEM

images of Au–Ag nanocubes, and setup for taking IR spectra. This material is available free of charge via the Internet at <http://pubs.acs.org>.

AUTHOR INFORMATION

Corresponding Author

*hyhuang@mx.nthu.edu.tw

Notes

The authors declare no competing financial interest.

ACKNOWLEDGMENTS

This work was funded by Ministry of Science and Technology of Taiwan (NSC 101-2113-M-007-018-MY3, MOST 102-2633-M-007-002, and MOST 103-2633-M-007-001).

REFERENCES

- (1) Auyeung, E.; Li, T. I. N. G.; Senesi, A. J.; Schmucker, A. L.; Pals, B. C.; de la Cruz, M. O.; Mirkin, C. A. *Nature* **2014**, *505*, 73–77.
- (2) Liao, C.-W.; Lin, Y.-S.; Chanda, K.; Song, Y.-F.; Huang, M. H. *J. Am. Chem. Soc.* **2013**, *135*, 2684–2693.
- (3) Shevchenko, E. V.; Talapin, D. V.; Murray, C. B.; O'Brien, S. J. *Am. Chem. Soc.* **2006**, *128*, 3620–3637.
- (4) Demortière, A.; Launois, P.; Goubet, N.; Albouy, P.-A.; Petit, C. J. *Phys. Chem. B* **2008**, *112*, 14583–14592.
- (5) Shen, X. S.; Wang, G. Z.; Hong, X.; Zhu, W. *CrystEngComm* **2009**, *11*, 753–755.
- (6) Xiao, J.; Li, Z.; Ye, X.; Ma, Y.; Qi, L. *Nanoscale* **2014**, *6*, 996–1004.
- (7) Chen, C.-J.; Chiang, R.-K.; Jeng, Y.-R. *J. Phys. Chem. C* **2011**, *115*, 18142–18148.
- (8) Xie, S.; Zhou, X.; Han, X.; Kuang, Q.; Jin, M.; Jiang, Y.; Xie, Z.; Zheng, L. *J. Phys. Chem. C* **2009**, *113*, 19107–19111.
- (9) Zhao, Z.; Zhang, J.; Dong, F.; Yang, B. *J. Colloid Interface Sci.* **2011**, *359*, 351–358.
- (10) Singh, A.; Ryan, K. M. *Part. Part. Syst. Charact.* **2013**, *30*, 624–629.
- (11) Talapin, D. V.; Shevchenko, E. V.; Kornowski, A.; Gaponik, N.; Haase, M.; Rogach, A. L.; Weller, H. *Adv. Mater.* **2001**, *13*, 1868–1871.
- (12) Zhu, Z.; Meng, H.; Liu, W.; Liu, X.; Gong, J.; Qiu, X.; Jiang, L.; Wang, D.; Tang, Z. *Angew. Chem., Int. Ed.* **2011**, *50*, 1593–1596.
- (13) Alvarez-Puebla, R. A.; Agarwal, A.; Manna, P.; Khanal, B. P.; Aldeanueva-Potel, P.; Carbó-Argibay, E.; Pazos-Pérez, N.; Vigderman, L.; Zubarev, E. R.; Kotov, N. A.; Liz-Marzán, L. M. *Proc. Natl. Acad. Sci. U.S.A.* **2011**, *108*, 8517–8161.
- (14) Gómez-Graña, S.; Pérez-Juste, J.; Alvarez-Puebla, R. A.; Guerrero-Martínez, A.; Liz-Marzán, L. M. *Adv. Opt. Mater.* **2013**, *1*, 477–481.
- (15) Tam, E.; Podsiadlo, P.; Shevchenko, E.; Ogletree, D. F.; Delplancke-Ogletree, M.-P.; Ashby, P. D. *Nano Lett.* **2010**, *10*, 2363–2367.
- (16) Yang, C.-W.; Chiu, C.-Y.; Huang, M. H. *Chem. Mater.* **2014**, *26*, 4882–4888.
- (17) Chiu, C.-Y.; Yang, M.-Y.; Lin, F.-C.; Huang, J.-S.; Huang, M. H. *Nanoscale* **2014**, *6*, 7656–7665.
- (18) Yang, C.-W.; Chanda, K.; Lin, P.-H.; Wang, Y.-N.; Liao, C.-W.; Huang, M. H. *J. Am. Chem. Soc.* **2011**, *133*, 19993–20000.
- (19) Tsao, Y.-C.; Rej, S.; Chiu, C.-Y.; Huang, M. H. *J. Am. Chem. Soc.* **2014**, *136*, 396–404.
- (20) Wu, J.-K.; Lyu, L.-M.; Liao, C.-W.; Wang, Y.-N.; Huang, M. H. *Chem.–Eur. J.* **2012**, *18*, 14473–14478.
- (21) Chiu, C.-Y.; Huang, M. H. *Angew. Chem., Int. Ed.* **2013**, *52*, 12709–12713.
- (22) Tang, M. L.; Liu, N.; Dionne, J. A.; Alivisatos, A. P. *J. Am. Chem. Soc.* **2011**, *133*, 13220–13223.
- (23) Chang, C.-C.; Wu, H.-L.; Kuo, C.-H.; Huang, M. H. *Chem. Mater.* **2008**, *20*, 7570.

- (24) Schaffer, M.; Schaffer, B.; Ramasse, Q. *Ultramicroscopy* **2012**, *114*, 62–71.
- (25) Haigh, S. J.; Gholinia, A.; Jalil, R.; Romani, S.; Britnell, L.; Elias, D. C.; Novoselov, K. S.; Ponomarenko, L. A.; Geim, A. K.; Gorbachev, R. *Nat. Mater.* **2012**, *11*, 764–767.
- (26) Raman, N. K.; Anderson, M. T.; Brinker, C. J. *Chem. Mater.* **1996**, *8*, 1682–1701.
- (27) Chen, P.-K.; Lai, N.-C.; Ho, C.-H.; Hu, Y.-W.; Lee, J.-F.; Yang, C.-M. *Chem. Mater.* **2013**, *25*, 4269–4277.
- (28) Fan, H.; Yang, K.; Boye, D. M.; Sigmon, T.; Malloy, K. J.; Xu, H.; López, G. P.; Brinker, C. J. *Science* **2004**, *304*, 567–571.
- (29) Jeng, U.-S.; Su, C. H.; Su, C.-J.; Liao, K.-F.; Chuang, W.-T.; Lai, Y.-H.; Chang, J.-W.; Chen, Y.-J.; Huang, Y.-S.; Lee, M.-T.; Yu, K.-L.; Lin, J.-M.; Liu, D.-G.; Chang, C.-F.; Liu, C.-Y.; Chang, C.-H.; Liang, K. S. *J. Appl. Crystallogr.* **2010**, *43*, 110–121.
- (30) Wu, W.-R.; Jeng, U.-S.; Su, C.-J.; Wei, K.-H.; Su, M.-S.; Chiu, M.-Y.; Chen, C.-Y.; Su, W.-B.; Su, C.-H.; Su, A.-C. *ACS Nano* **2011**, *5*, 6233–6243.
- (31) Sau, T. K.; Murphy, C. J. *Langmuir* **2005**, *21*, 2923–2929.
- (32) Gómez-Graña, S.; Hubert, F.; Testard, F.; Guerrero-Martínez, A.; Grillo, I.; Liz-Marzán, L. M.; Spalla, O. *Langmuir* **2012**, *28*, 1453–1459.
- (33) Young, K. L.; Personick, M. L.; Engel, M.; Damasceno, P. F.; Barnabym, S. N.; Bleher, R.; Li, T.; Glotzer, S. C.; Lee, B.; Mirkin, C. A. *Angew. Chem., Int. Ed.* **2013**, *52*, 13980–13984.
- (34) Damasceno, P. F.; Engel, M.; Glotzer, S. C. *ACS Nano* **2011**, *6*, 609–614.
- (35) Damasceno, P. F.; Engel, M.; Glotzer, S. C. *Science* **2012**, *337*, 453–457.
- (36) Kuo, C.-H.; Yang, Y.-C.; Gwo, S.; Huang, M. H. *J. Am. Chem. Soc.* **2011**, *133*, 1052–1057.
- (37) Tan, C.-S.; Hsiao, C.-H.; Wang, S.-C.; Liu, P.-H.; Lu, M.-Y.; Huang, M. H.; Ouyang, H.; Chen, L.-J. *ACS Nano* **2014**, *8*, 9422–9426.
- (38) Chen, C.-K.; Chang, M.-H.; Wu, H.-T.; Lee, Y.-C.; Yen, T.-J. *Biosens. Bioelectron.* **2014**, *60*, 343–350.
- (39) Chen, C.-F.; Tzeng, S.-D.; Chen, H.-Y.; Lin, K.-J.; Gwo, S. *J. Am. Chem. Soc.* **2008**, *130*, 824–826.
- (40) Zhao, Q.; Zhou, J.; Zhang, F.; Lippens, D. *Mater. Today* **2009**, *12*, 60–69.
- (41) Haigh, S. J.; Gholinia, A.; Jalil, R.; Romani, S.; Britnell, L.; Elias, D. C.; Novoselov, K. S.; Ponomarenko, L. A.; Geim, A. K.; Gorbachev, R. *Nat. Mater.* **2012**, *11*, 764–767.